RESEARCH ARTICLE

NANO · MICRO small
www.small-journal.com

Spatial Effect on the Performance of Carboxylate Anode Materials in Na-Ion Batteries

Jinghao Huang, Shi Li, You Wang, Eric Youngsam Kim, Zhenzhen Yang, Dongchang Chen, Lei Cheng,* and Chao Luo**

Developing low-voltage carboxylate anode materials is critical for achieving low-cost, high-performance, and sustainable Na-ion batteries (NIBs). However, the structure design rationale and structure-performance correlation for organic carboxylates in NIBs remains elusive. Herein, the spatial effect on the performance of carboxylate anode materials is studied by introducing heteroatoms in the conjugation structure and manipulating the positions of carboxylate groups in the aromatic rings. Planar and twisted organic carboxylates are designed and synthesized to gain insight into the impact of geometric structures to the electrochemical performance of carboxylate anodes in NIBs. Among the carboxylates, disodium 2,2'-bipyridine-5,5'-dicarboxylate (2255-Na) with a planar structure outperforms the others in terms of highest specific capacity (210 mAh g^{-1}), longest cycle life (2000 cycles), and best rate capability (up to 5 A g^{-1}). The cyclic stability and redox mechanism of 2255-Na in NIBs are exploited by various characterization techniques. Moreover, high-temperature (up to 100 °C) and all-organic batteries based on a 2255-Na anode, a polyaniline (PANI) cathode, and an ether-based electrolyte are achieved and exhibited exceptional electrochemical performance. Therefore, this work demonstrates that designing organic carboxylates with extended planar conjugation structures is an effective strategy to achieve high-performance and sustainable NIBs.

1. Introduction

Due to the ever-increasing demands for consumer electronics, electric vehicles, and stationary energy storage, it is paramount to develop cost-effective, environmentally benign, and sustainable energy storage devices as alternatives to lithium-ion batteries (LIBs).[1–5] Among state-of-the-art rechargeable batteries, Na-ion batteries (NIBs) stand out because of high abundance, low cost, and high sustainability of sodium resources, as well as the similar physicochemical properties of Na ions to Li ions.[6–7] However, due to the larger ion size and more complicated intercalation chemistry of Na ions, most high-performance electrode materials in LIBs such as graphite, silicon, transition metal oxides, etc. do not extend their performance to NIBs. The capacity, energy density, and lifetime of NIBs are still not comparable to LIBs.[8–10] Therefore, it is critical to search for low-cost, abundant, sustainable, and high-performance materials for advanced NIBs.

Among various electrode materials in NIBs, organic electrode materials (OEMs) consisting of light elements such as C, H, O, N, S are promising candidates because of their high sustainability, abundant structural diversity, and flexible structural tunability.[11–22] To date, there are five types of reaction mechanisms in organic NIBs, including carbonyl (C = O), imine (C = N), azo (N = N), thioketone/thioester (C = S), and anion insertion reactions. Among them, the carboxylate-based carbonyl reaction, Schiff base-based imine reaction, and

J. Huang, E. Y. Kim, C. Luo
Department of Chemistry and Biochemistry
George Mason University
Fairfax, VA 22030, USA
E-mail: cluo@gmu.edu

S. Li
Material Science Division
Argonne National Laboratory
Lemont, Illinois 60439, USA

Y. Wang, D. Chen
Department of Chemistry and Chemical Biology
University of New Mexico
Albuquerque, NM 87131, USA
E-mail: chend@unm.edu

Z. Yang
Chemical Sciences and Engineering Division
Argonne National Laboratory
Lemont, IL 60439, USA

L. Cheng
Chemical Sciences Division
Oak Ridge National Laboratory
Oak Ridge, TN 37831, USA
E-mail: chengl@ornl.gov

C. Luo
Quantum Science & Engineering Center
George Mason University
Fairfax, VA 22030, USA

The ORCID identification number(s) for the author(s) of this article can be found under https://doi.org/10.1002/smll.202308113

DOI: 10.1002/smll.202308113

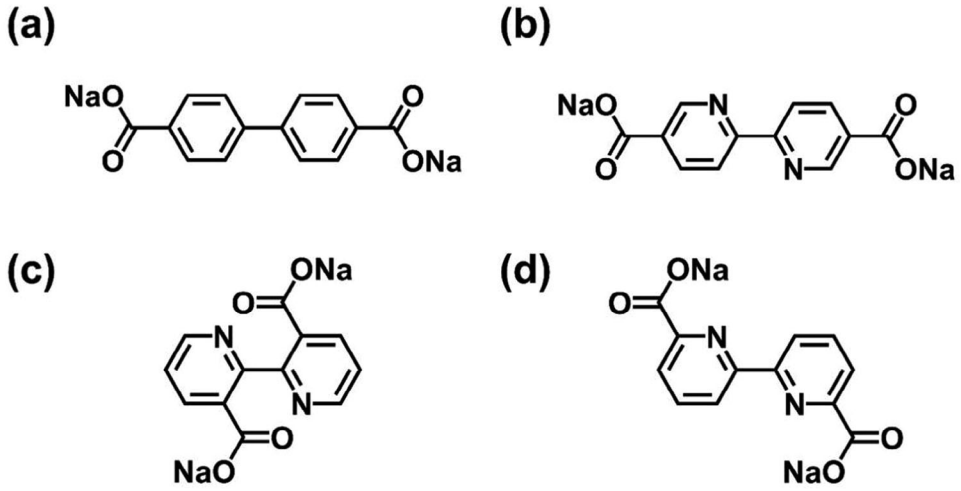

Figure 1. Molecular structures of a) BPDC-Na, b) 2255-Na, c) 2233-Na, d) 2266-Na.

azo reaction exhibit relatively low redox potentials in NIBs, offering opportunities for developing high-performance organic anodes.[23–27] However, the redox potentials of azo compounds are centered at ≈1.3 V in NIBs, which is high for anodes.[28] Schiff bases show redox plateaus at 0.5–1.2 V but moderate cyclic stability.[29,30] Among various organic anodes, carboxylate compounds are promising because of their low redox potentials (<1.0 V), high specific capacity, and long cycle life.[31–35] Due to abundant and diverse nature of carboxylate compounds, their molecular structures are highly tunable and can be easily tailored to improve the electrochemical performance for sustainable NIBs.[36–38]

Though carboxylates are promising anode materials, they suffer from low electronic conductivity and high solubility in the electrolytes, resulting in low utilization of active materials and rapid capacity lost upon cycling. To address these challenges, rational structure design of carboxylates to enhance the conductivity and reduce the solubility is essential, so a fundamental understanding toward the structure-performance correlation is demanded. As well-documented, extending the conjugated structures and salt formation are effective strategies to simultaneously increase electronic conductivity and reduce the solubility due to the increased π-aromatic conjugation and molecular polarity.[39–43] Fluorination of the aromatic ring in the disodium terephthalate can improve the stability of sodiated intermediates and products by forming ion-dipole interactions between Na ions and F atoms.[44] Structure isomerism by manipulating the positions of carboxylate groups in the aromatic ring alters the electronic structure and polarity of carboxylates, leading to enhanced electrochemical performance. Nevertheless, the impact of the other factors such as the spatial structure remains elusive. Bo, et al. reported a carboxylate acid, 2, 2'-bipyridine-5, 5'-dicarboxylic acid as the organic anode material of NIBs.[45] The material was proved to have a planar molecular structure. However, the acid is soluble in the liquid organic electrolytes, leading to capacity loss. To mitigate the dissolution, it is essential to develop the corresponding sodium carboxylate salt to optimize the performance and study the spatial effect. The spatial structure of carboxylates influences the electrochemical reactions by varying steric hinderance and electron transfers. Therefore, it is vital to gain insight into the effect of spatial structures of carboxylates on their electrochemical performance and offer guidance for rational structure design and performance optimization of carboxylate anodes in NIBs.

Herein, we synthesized three sodium carboxylates with N-doped conjugated structures as follows: disodium 2, 2'-bipyridine-3, 3'-dicarboxylate (2233-Na), disodium 2, 2'-bipyridine-5, 5'-dicarboxylate (2255-Na), disodium 2, 2'-bipyridine-6, 6'-dicarboxylate (2266-Na). They have the same backbone structure (bipyridine rings) and functional group (carboxylate group). The main difference in the molecular structure is the positions of functional groups in the aromatic rings (**Figure 1**). Moreover, another carboxylate anode material, disodium 4,4'-biphenyl dicarboxylate (BPDC-Na), was employed as a control sample to compare with 2233-Na, 2255-Na, and 2266-Na. As confirmed by the computational results, 2255-Na and 2266-Na show the planar structure, while 2233-Na and BPDC-Na exhibit the twisted structure. In NIBs, planar 2255-Na shows the best electrochemical performance in terms of highest specific capacity (210 mAh g^{-1}), longest cycle life (2000 cycles), and highest rate capability (up to 5 A g^{-1}). However, the twisted 2233-Na and BPDC-Na suffer from fast capacity decay. The planar 2266-Na also suffers from fast capacity decay due to its solubility in the electrolyte. Since 2255-Na shows the best performance, it is also coupled with a polyaniline (PANI) cathode to make the all-organic full cells, which show outstanding performance at room temperature and high temperatures (up to 100 °C).

Commercial Li-ion batteries have an operation temperature window ranging from −20 to +60 °C, limiting the applications in well drilling industry, and high temperature regions such as deserts, equatorial areas, etc. The development of high-temperature batteries at up to 100 °C is pivotal to expand large-scale applications of energy storage devices under extreme conditions. However, the inferior structure integrity of electrode materials during fast ion/electron transfer and unstable electrolytes/interphases at high temperatures compromise the performance of high-temperature batteries. To address this

challenge, an ether-based electrolyte was designed and showed high performance in high-temperature batteries. In this work, we not only developed a stable carboxylate anode (2255-Na) but also coupled it with a stable PANI cathode and a high-boiling-point ether-based electrolyte to construct all-organic high-temperature batteries, aiming to expand the applications of next-generation energy storage devices to the fields requiring high operation temperatures.

2. Results and Discussions

The three positional isomers, 2255-Na, 2233-Na, and 2266-Na, have similar structures with the control sample, BPDC-Na. However, due to the different conjugation structures or functional groups' positioning in the conjugation structures, their spatial structures are different. To understand this, we performed density functional theory (DFT) calculations of all four molecules using Gaussian 16 to determine the potential energy surface.[46] **Figure** 2a shows the potential energy surface (PES) of the four monomers, with the corresponding dihedrals highlighted in red. Both bipyridine- and biphenyl-type molecules have one stable conformer. When the carboxylate group is attached to the 5 or 6 position of the pyridine, the low-energy conformer has a dihedral angle of 180 degrees, indicating a planar conformation of the molecule. Conversely, when the carboxylate group is at position 3 of the pyridine, the dihedral angle of the low-energy conformer is ≈40 degrees, indicating a twisted backbone of the monomer. The biphenyl type molecule also exhibits a twisted backbone when the carboxylate group is at the position 4 with a dihedral angle of 40 degrees.

The stable conformation of each molecule with disodium salt was further confirmed through the geometry optimization, as shown in Figure 2b. The twist backbone of BPDC-Na can be partially attributed to steric hindrance of the two hydrogen atoms on the adjacent carbon in the benzene ring, which causes the repulsion between the two hydrogen atoms. Another reason for the twisted conformation is the relatively small rotational energy barrier between the two phenyl groups, which is 0.12 eV compared to 0.4 eV for the bipyridine-type monomers. Consequently, the biphenyl rotates around the C-C' axis and has a minimum energy barrier of approximately 40 degrees. In 2255-Na and 2266-Na, the repulsion between the nitrogen atoms is minimized in the planar conformation.

The different conformation of the four monomers can be further explained through frontier molecular orbital analysis shown in Figure S1 (Supporting Information). In 2255-Na and 2266-Na, the highest-occupied molecular orbital (HOMO) is mostly localized on the bipyridine rings. The overlap of π-orbitals in the two pyridine rings creates a conjugated system of electrons that allows the delocalization of the π-electrons throughout the molecule, thereby lowering the energy of the molecule's planar conformation. In 2233-Na, the HOMOs extend to the carboxylate groups, steric hindrance of the carboxylate groups results in high energy barrier that prevents the molecule from forming a planar conformation. Thus, according to the calculation results, we predict that despite the structures of these positional isomers are similar, their electrochemical performances should be different because of their different spatial conformations. To confirm our prediction, multiple experiments were proceeded to test their performances in NIBs.

The as-synthesized four organic anode materials, 2255-Na, 2233-Na, 2266-Na, and BPDC-Na were characterized by a variety of characterization techniques, including Fourier-transform infrared spectroscopy (FTIR), X-ray diffraction (XRD), UV-vis spectroscopy, Raman spectroscopy, and scanning electron microscopy (SEM). Based on the FTIR spectrum of 2255-Na (**Figure** 3a), the sharp peaks at 1406 cm^{-1} and 1582cm^{-1} represent the symmetric and asymmetric stretching vibration of carboxylate groups in 2255-Na, respectively.[47] These peaks also appear in the FTIR spectra of the other three compounds (Figures S2a,S3a, and S4a, Supporting Information). This observation illustrates the presence of the carboxylate group in all the organic materials. To verify the results, Raman tests were utilized to measure the four anode materials. As shown in Figure 3b, the peaks at 1628 cm^{-1} and 1406 cm^{-1} represent the asymmetric and symmetric stretching vibrations of the carboxylate group.[48] For 2233-Na (Figure S2b, Supporting Information), 2266-Na (Figure S3b, Supporting Information), and BPDC-Na (Figure S4b, Supporting Information), the stretching vibration peaks for the carboxylate group can also be observed, which further proves the presence of carboxylate groups in the four organic materials. In addition, the Raman spectra of 2255-Na and 2266-Na show obvious sloping baselines due to the fluorescence emitted by their planar aromatic structures, while the Raman spectra of 2233-Na and BPDC-Na do not indicate strong fluorescence because of their twisted structures.[49,50] The XRD technique was employed to study the crystal structures of materials. In Figure 3c and Figures S2c,S3c,S4c (Supporting Information), all these organic carboxylate compounds display crystalline structures. The peaks at 36.7, 42.9, and 63.3° come from the background (the sample holder). In a previous literature, researchers reported the XRD pattern of 2,2'-bipyridine-5,5'-dicarboxylic acid, which exhibited three peaks at 17.2°, 24.9°, and 27.8° for the (011), (101), and (110) planes, respectively.[45] They proved that the molecules adopt a lamellar packing motif, indicating the planar molecular structure. In the XRD pattern of 2255-Na (Figure 3c), it shows three peaks at similar positions (16.7, 24.8, and 27.2°), proving that 2255-Na molecules also adopt lamellar packing. Similarly, the XRD pattern of 2266-Na also has similar peaks, while the XRD peaks of 2233-Na and BPDC-Na are different. These results demonstrate that 2255-Na and 2266-Na have planar structures, while 2233-Na and BPDC-Na exhibit twisted structures. To further confirm the structure, we also performed a UV–vis test of the four compounds. The spectra are shown in Figure S6 (Supporting Information). The absorption peaks of 2255-Na (314 nm) and 2266-Na (300 nm) were at higher wavelength than those of 2233-Na (256 nm) and BPDC-Na (273 nm), indicating a smaller HOMO–LUMO energy gap of 2255-Na and 2266-Na.[51] The smaller energy gaps imply a larger π-conjugated system. Since the four molecules have similar molecular structure, the larger π-conjugated system suggests that 2255-Na and 2266-Na exhibit planar structures, while 2233-Na and BPDC-Na with smaller π-conjugated system exhibit twisted structures.

To further exploit the structure of the 2255-Na, X-ray photoelectron spectroscopy (XPS) was utilized to measure the 2255-Na powder. As shown in Figure 3d, the peak at 284.7 eV for the graphitic carbon in the C 1s spectrum of the 2255-Na powder is

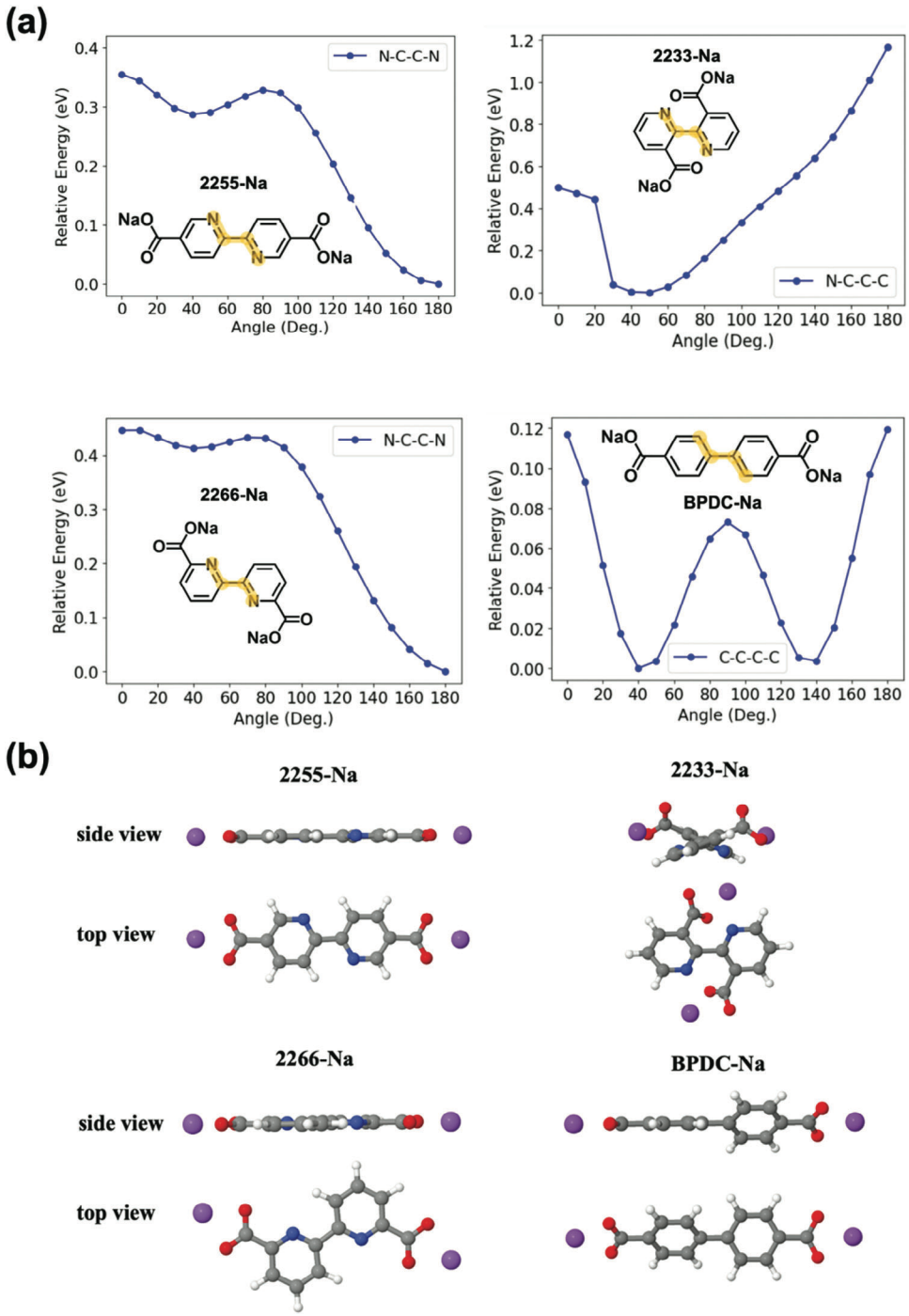

Figure 2. a) Computed potential energy surface for four monomers with respect to the X–C–C'–X dihedral angle (marked in red) at wB97X-D/6-311++G(d,p) level of theory. b) Side and top view of the optimized structure of four monomers determined at wB97X-D/6-311++G(d,p) level of theory. The carbon, nitrogen, and oxygen atoms are represented by gray, blue, and red colors, respectively, while sodium and hydrogen atoms are denoted by purple and white colors, respectively.

used as a reference peak. The peaks at 285.5 eV and 288.2 eV stand for the C-O (from the sodium alginate binder) and -COO^- group, respectively.[52] The peak at 286.9 eV represents the C = N-C group. In the N 1s spectrum, the peak at 398.8 eV indicates the existence of the imine group. In the O 1s spectrum, the peaks at 530.8 eV and 531.7 eV stand for the -COO^- group and -OH group (from the sodium alginate binder), respectively. Thus, the spectra of XPS proves the presence of functional groups in 2255-Na. To further study the molecular structure of these three carboxylate compounds, ^{1}H NMR and ^{13}C NMR were applied for

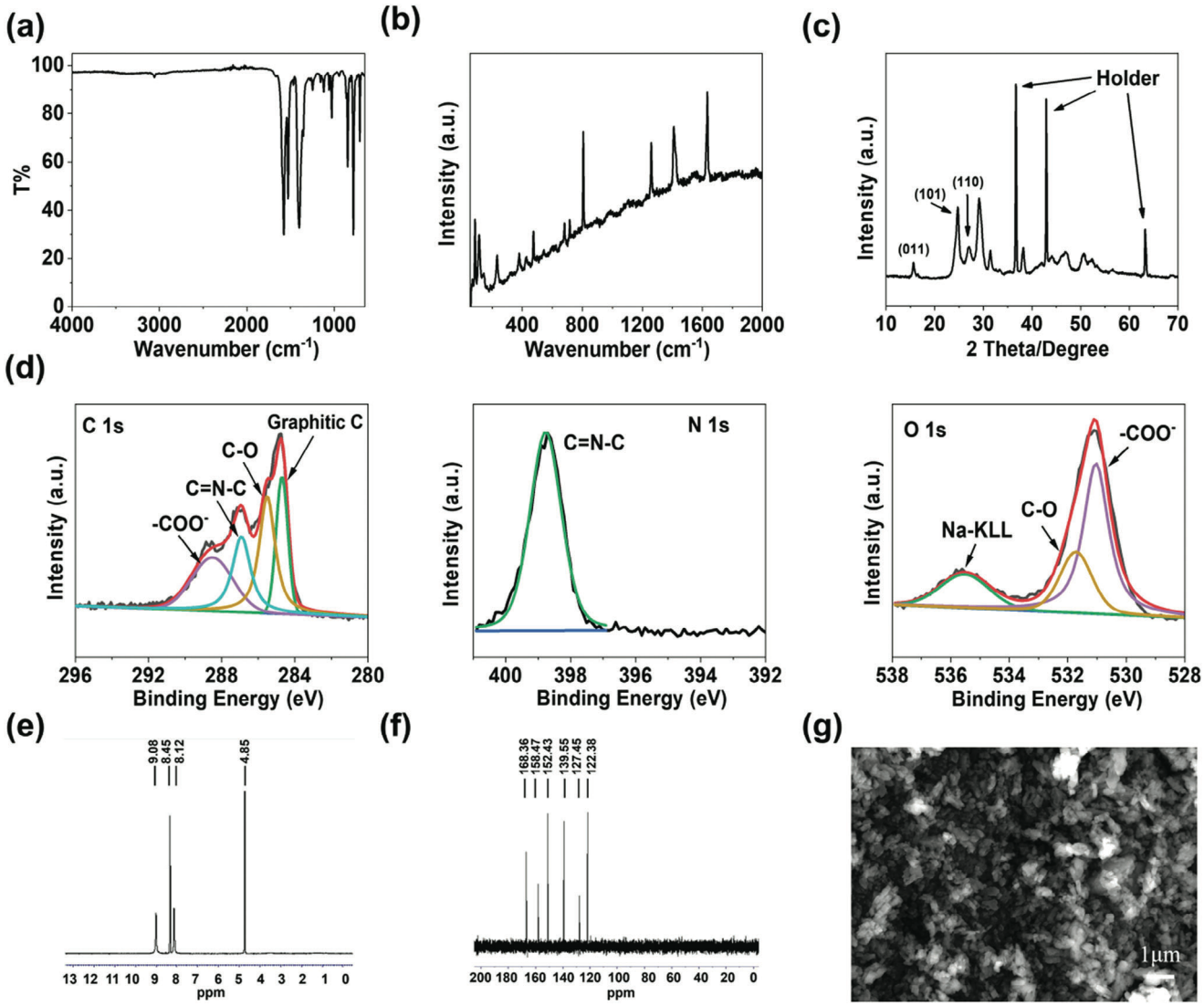

Figure 3. Characterization results of 2255-Na. a) FTIR spectrum, b) Raman spectrum, c) XRD pattern, d) C 1s, N 1s, and O 1s XPS spectra of the 2255-Na powder, e) ^{1}H NMR spectrum, f) ^{13}C NMR spectrum, g) SEM image.

characterization with Deuterium oxide (D_2O) as the solvent. Based on the ^{1}H NMR spectrum of 2255-Na (Figure 3e), the peak at 8.12, 8.45, and 9.08 ppm indicates the three types (totally six) of hydrogen atoms attached to the pyridine ring of 2255-Na.[53] In the ^{13}C NMR spectrum (Figure 3f), the peak at 168.36 ppm represents the sp^2 carbons in the carboxylate groups, while the peaks at 122.38, 127.45, 139.55, 152.43, and 158.47 ppm are attributed to the aromatic carbons in the pyridine ring. Similarly, the ^{1}H and ^{13}C NMR spectra of 2233-Na (Figure S2d,e, Supporting Information) and 2266-Na (Figure S3d,e, Supporting Information) also demonstrate their molecular structures. In the ^{1}H and ^{13}C NMR spectra of BPDC-Na (Figure S4d,e, Supporting Information), it has two proton peaks in the chemical shift from 7–8 ppm and five carbon peaks from 120–180 ppm owing to its symmetric molecular structure, aromatic rings, and carboxylate groups. To confirm the structures of 2255-Na, 2233-Na, and 2266-Na, mass spectroscopy (MS) tests were carried out to measure their molecular weight. As shown in Figure S5 (Supporting Information), the MS results of 2255-Na, 2233-Na, and 2266-Na are all close to 288 g mol^{-1}, which are well matched with their calculated molecular weight. These results demonstrates that the three positional isomers were successfully synthesized. The morphology of the three isomers and the control sample is observed by SEM. As shown in Figure 3g and Figures S2f,S3f, and S4f (Supporting Information), the 2255-Na particle size is in the submicrometer to micrometer range. These results confirmed the molecular structures of the four compounds containing carboxylate groups, and they are all composed of micron-sized particles.

To exploit the electrochemical performance of the three positional isomers and the control sample, these compounds were used as active materials in the anodes and coupled with the sodium metal as the counter electrode in NIBs. As shown in the galvanostatic charge-discharge curves (**Figure 4a**), 2255-Na delivered an initial charge capacity of 210 mAh g^{-1} at the current

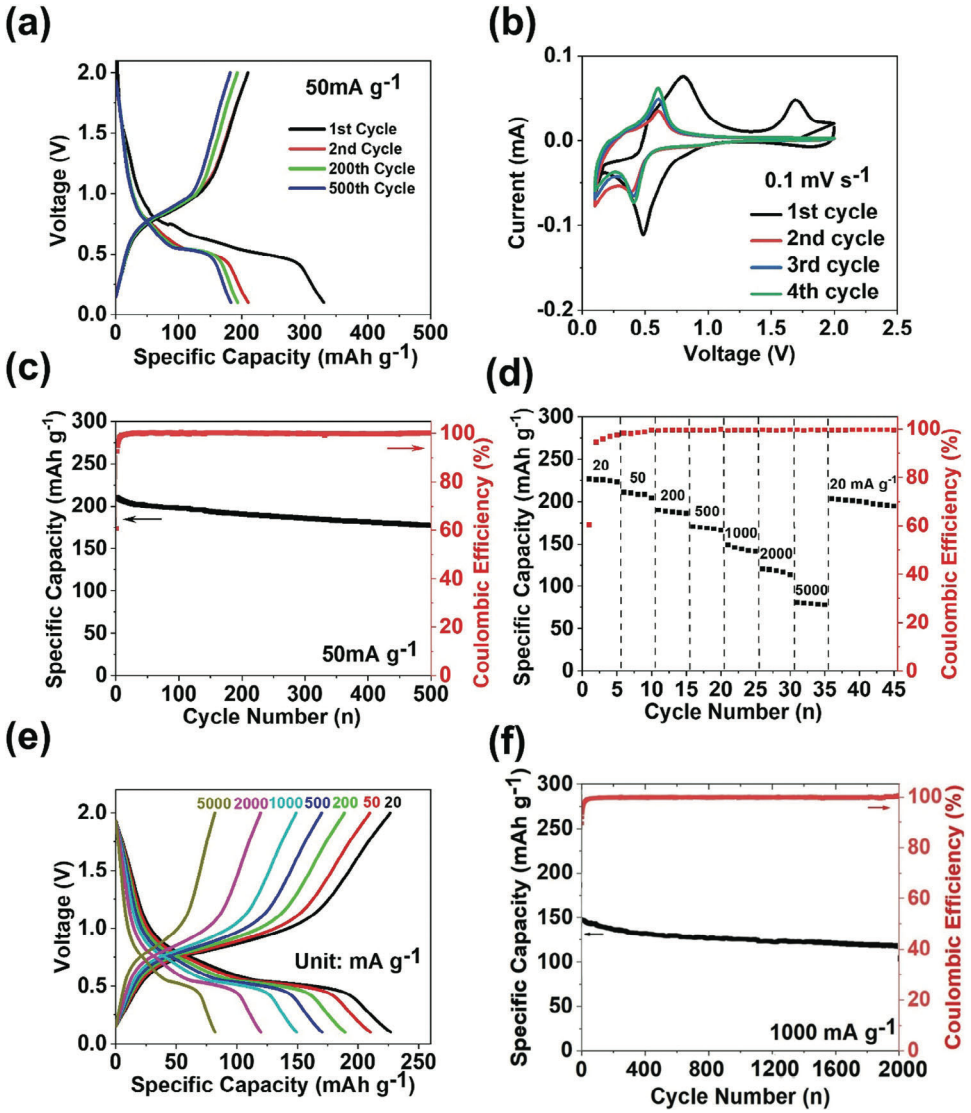

Figure 4. Electrochemical performances of 2255-Na in NIBs. a) Galvanostatic charge-discharge curves at 50 mA g^{-1}, b) CV curves at the scan rate of 0.1 mV s^{-1}, c) cycle life and Coulombic efficiency at the current density of 50 mA g^{-1}, d) Galvanostatic charge-discharge curves at different current densities from 20 to 5000 mA g^{-1}, e) rate capability result at various current densities, f) cycle life and Coulombic efficiency at the current density of 1A g^{-1}.

density of 50 mA g^{-1} with a pair of redox plateaus centered at 0.52 V. However, the Coulombic efficiency (CE) of the first cycle is only 60% due to the formation of the solid electrolyte interface (SEI) in the first cycle.[23] To exclude the capacity contribution from carbon black, the reversible capacity of carbon black was measured at 100 mA g^{-1} because the ratio of carbon black to 2255-Na is 1:2 in the electrode, and the current density for 2255-Na anode is 50 mA g^{-1}. The carbon black electrode showed a reversible capacity of 38.8 mAh g^{-1} (Figure S7, Supporting Information). The capacity contribution of carbon black was subtracted from the capacity of 2255-Na, and cycle life and Coulombic efficiency of 2255-Na without carbon black contribution is presented in Figure S8 (Supporting Information). From the cyclic voltammetry (CV) curves (Figure 4b), the anodic peak of 2255-Na is at 0.62 V, while the cathodic peak is at 0.48 V, which are consistent with the redox plateaus in the galvanostatic charge-discharge curves (Figure 4a). The performance at the first cycle is different from the subsequent cycles, because of the material phase change and electrode-electrolyte interphase formation during the first cycle. As evidenced by Figure S11b (Supporting Information), the pristine 2255-Na anode shows a sharp peak at 29 degree in the XRD pattern, and its intensity is significantly reduced after 1st cycle, demonstrating the material phase change. It causes the irreversible anodic peak at 1.7 V in the first cycle, and both cathodic and anodic peaks shift to lower voltage values after the first cycle. In addition, the formation of SEI during the first cycle enhances the cathodic peak intensity during the first discharge.

In contrast, 2233-Na, 2266-Na, and BPDC-Na displayed initial charge capacities and first cycle CEs of 49 mAh g^{-1}, 38% (Figure S9a,d, Supporting Information), 156 mAh g^{-1}, 39%

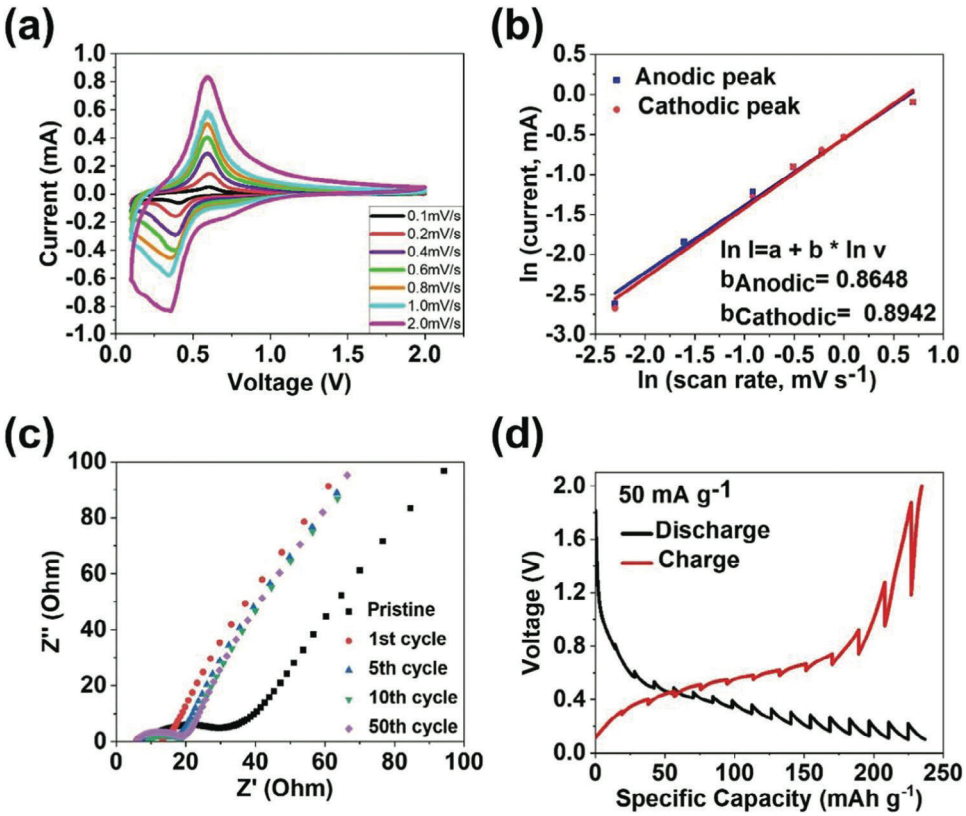

Figure 5. Reaction kinetics of 2255-Na. a) CV curves at various scan rates from 0.1 to 2.0 mV s^{-1}, b) the relationship between natural logarithm of scan rates and the corresponding peak currents, c) EIS tests of pristine electrode and electrodes after different cycles, d) GITT test at the current density of 50 mA g^{-1}.

(Figure S9b,e, Supporting Information), and 208mAh g^{-1}, 58% (Figure S9c,f, Supporting Information) at 50 mA g^{-1}, respectively, which are lower than those of 2255-Na. In the long-term cyclic stability results, 2255-Na retains a reversible capacity of 178 mAh g^{-1} at 50 mA g^{-1} after 500 cycles (Figure 4c), corresponding to a very slow capacity decay rate of 0.03% per cycle. In addition, the CE of 2255-Na is close to 100% upon long-term cycling. In contrast, BPDC-Na retains 135 mAh g^{-1} at 50 mA g^{-1} after 300 cycles (Figure S9f, Supporting Information) with a capacity decay rate of 0.29% per cycle. 2233-Na (Figure S9d, Supporting Information) and 2266-Na (Figure S9e, Supporting Information) also show low capacity and poor capacity retention upon long-term cycling. Based on the results, 2255-Na showed both highest reversible capacity and highest cyclic stability, demonstrating the best anode material among the four carboxylate compounds. The previous tests were conducted based on the 2255-Na anode with Cu as the current collector, and we also tested the 2255-Na anode with Al foil as the current collector. As shown in Figure S10 (Supporting Information), the 2255-Na anode with Al foil as the current collector exhibits similar electrochemical behaviors as that with Cu foil as the current collector, demonstrating that the current collectors do not impact the performance. Since Al is more abundant and cost-effective than Cu, Al foil should be used as the current collector in NIBs. Figure 4d shows rate capability of 2255-Na at various current densities from 20 mA g^{-1} to 5 A g^{-1}, and Figure 4e shows the galvanostatic charge-discharge curves of 2255-Na at different current densities. The current density is increased from 20 mA g^{-1} to 5 A g^{-1}, and the capacity is reduced from 225 mAh g^{-1} to 79 mAh g^{-1}. When the current density is decreased back to 20 mA g^{-1}, the reversible capacity recovers to 203 mAh g^{-1} with the capability recovery of 90%, demonstrating robust rate capability. Due to the exceptional rate performance, a high current density of 1A g^{-1} was applied for a high-rate and long cycling test. As shown in Figure 4f, 2255-Na can retain a reversible capacity of 123.3 mAh g^{-1} at 1A g^{-1} after 2000 cycles, demonstrating excellent cycling stability and fast-charging capability in NIBs.

To further study the reaction kinetics of 2255-Na, CV tests at various scan rates, electrochemical impedance spectroscopy (EIS), and galvanostatic intermittent titration technique (GITT) were employed. As shown in **Figure 5**a, the cell with 2255-Na was scanned from 0.1 mV s^{-1} to 2.0 mV s^{-1}. The peak currents at different scan rates were obtained, and the relationship between natural logarithm of scan rates and the corresponding peak currents was plotted. The linear fits of relationships of anodic and cathodic peak are shown in Figure 5b. The b values of cathodic and anodic peaks are 0.8942 and 0.8648, respectively. Since the slope values are close to 1, the partial capacitive behavior dominates the redox reaction of the 2255-Na anode, contributing to the high rate capability.[54] In Figure 5c, the EIS test results show that the interfacial resistance of the pristine 2255-Na anode represented by the depressed semi-circle is ≈30 Ohm. It is reduced to 15 Ohm

after the first cycle and gradually increased to 16 Ohm after 10 cycles. The interfacial resistance was stabilized at 19 Ohm after 50 cycles. The small and stable interfacial resistance upon cycling indicates the stable SEI layer in the 2255-Na anode, which is critical for the high cyclic stability. Figure 5d displays the results of the GITT test. The charge and discharge potentials of 2255-Na are centered at 0.6 V and 0.4 V, respectively. In the regions of charge and discharge plateaus, the overpotentials are 32 mV and 45 mV, respectively. These small overpotentials further indicate the fast reaction kinetics of the 2255-Na anode.

To exploit the interfacial structure of the 2255-Na anode, XPS was utilized to measure the pristine 2255-Na anode, and cycled 2255-Na anodes at different charge and discharge stages. As shown in **Figure 6**a, the peak at 284.7 eV for the graphitic carbon in the C 1s spectrum of the 2255-Na pristine electrode is used as a reference peak. The peaks at 285.7 eV and 288.3 eV stand for the C-O and -COO^- group, respectively. The peak at 286.5 eV represents the C = N-C group. In the C 1s spectra (Figure 6b) of the 2255-Na anode discharged to 0.5 V, the C = N-C peak disappeared, and a new peak at 290 eV, which represents the C-F group formed in the solid electrolyte interphase (SEI). The fluorine comes from the decomposition of $NaPF_6$, and the C = N-C peak is overlapped by other peaks from the SEI. According to Figure 6b–e, the intensity of the C-F peak increases in C 1s spectra during the first discharge and charge, indicating the increase of fluorine compounds in the SEI. According to the N 1s spectra in Figure 6a–e, the peak for the imine group does not change, proving that the imine groups in the pyridine rings of 2255-Na did not involve in the redox reaction and SEI formation. To further investigate the fluorine compounds, the F 1s XPS spectra were also analyzed. In the XPS spectrum for F 1s of the pristine 2255-Na anode (Figure 6a), no fluorine is shown in the pristine electrode. After cycling, two F 1s peaks at 687.1 and 684.0 eV appear (Figure 6b–e), representing C-F and Na-F in the SEI layer, respectively. Moreover, the peak ratio of Na-F to C-F in the 2255-Na anode increases with the SEI formation, indicating a higher proportion of NaF content in the SEI layer. Since NaF is a very stable component in the SEI layer, a higher NaF content enhances the stability of the SEI layer, which contributes to long cycle life of the 2255-Na anode.

To further investigate the molecular, crystalline, and morphological structure change after cycling, FTIR, XRD, and SEM were utilized to measure the pristine and cycled 2255-Na anodes. As shown in Figure S11a (Supporting Information), the peaks in FTIR spectra are the same as the pristine 2255-Na anode to the anode after 20 cycles, which indicates that the molecular structure of 2255-Na is stable during the cycling process. Figure S11b (Supporting Information) shows the XRD patterns of pristine and cycled 2255-Na anodes. The peak at 29 degree of cycled spectra shows much lower intensity than that in the XRD pattern of the pristine anode. The intensity decrease of the XRD peak at 29 degree is due to the phase change of the crystal structure after the intercalation/extraction of Na ions during the first cycle. Figure S11c–f (Supporting Information) shows the SEM images of 2255-Na anodes from pristine to 10th cycle. It can be observed that the shape and size of 2255-Na particles did not change during cycling, which further proves the high stability of 2255-Na in NIBs.

Based on the computational and experimental results, the difference of electrochemical properties of the four compounds is related to their spatial structures. For 2233-Na, since the two carboxylate groups are too close with each other, it suffers from high steric hinderance during the sodiation/de-sodiation process. Thus, 2233-Na only provides low reversible capacity in NIBs (Figure S9a,d, Supporting Information). Compared to twisted BPDC-Na, 2255-Na and 2266-Na have a planar conformation, enabling an extended delocalized π-conjugation structure and the aromaticity of the two pyridine rings. This not only stabilizes the structures of 2255-Na and 2266-Na but also facilitates electron transfer, resulting in high cyclic stability and fast reaction kinetics. However, as evidenced by SEM images in Figure S12 (Supporting Information), the 2266-Na anode forms more large pores after cycling due to the dissolution of 2266-Na in the electrolyte. The solubility of 2266-Na in the electrolyte causes the capacity loss upon cycling. Therefore, 2255-Na with a planar conformation represents the best organic anode materials in NIBs among the four carboxylate compounds.

Since the 2255-Na anode exhibits superior electrochemical performance in NIBs, we also assessed its performance in K-ion batteries (KIBs). We prepared the potassium salt of 2, 2'-bipyridine-5, 5'-dicarboxylic acid (2255-K) using the same method for the sodium salts as described in the experimental section and tested it in KIBs. Figures S13 and S14 (Supporting Information) show the material characterization results of 2255-K, confirming its molecular structure and morphology. A 2.8 M KPF_6 in diethylene glycol dimethyl ether (DEGDME) electrolyte was used in the battery test, since it showed excellent performance for KIBs in our previous study.[48] As shown in Figure S15a,b (Supporting Information), 2255-K delivers an initial capacity of 170 mAh g^{-1} at current density of 50 mA g^{-1} and retains a reversible capacity of 135 mAh g^{-1} after 200 cycles, demonstrating high capacity and cyclic stability in KIBs. The results indicate that 2255-K is also a promising anode material in stable and sustainable KIBs.

Since both sodium and potassium salt of 2, 2'-bipyridine-5, 5'-dicarboxylic acid (2255-Na and 2255-K) exhibited excellent performance in alkaline-ion batteries. We further investigated the reaction mechanism. **Figure 7**a shows the proposed reaction mechanism of 2255-Na/K salts. Though the π-conjugation of 2255-Na does not store Na ions during the electrochemical redox reaction, intramolecular electron transfer takes place in the π-conjugation structure as shown in Figure 7a, resulting in the rearrangement of carbon-carbon and carbon-nitrogen double bonds in the conjugation structure. This will impact the structure stability and solubility of the reaction intermediates and products. The planar π-conjugation structure enables the aromaticity of 2255-Na, which enhances the structure stability and facilitates electron transfer. Therefore, the planar 2255-Na exhibits high cyclic stability and fast reaction kinetics. We employed *operando* Raman spectroscopy to investigate the redox mechanism by interrogating the changes of vibration bands as a various stage of charge/discharge. Raman spectroscopy is based on inelastic scattering between incident photons and vibration modes of molecules or crystals. It has been well known that the type and chemical environment of organic functional groups can lead to rich vibrational features,[55] which make operando Raman ideally suited for this study. Here, operando Raman spectroscopy was performed for three consecutive cycles. Figure 7b shows the

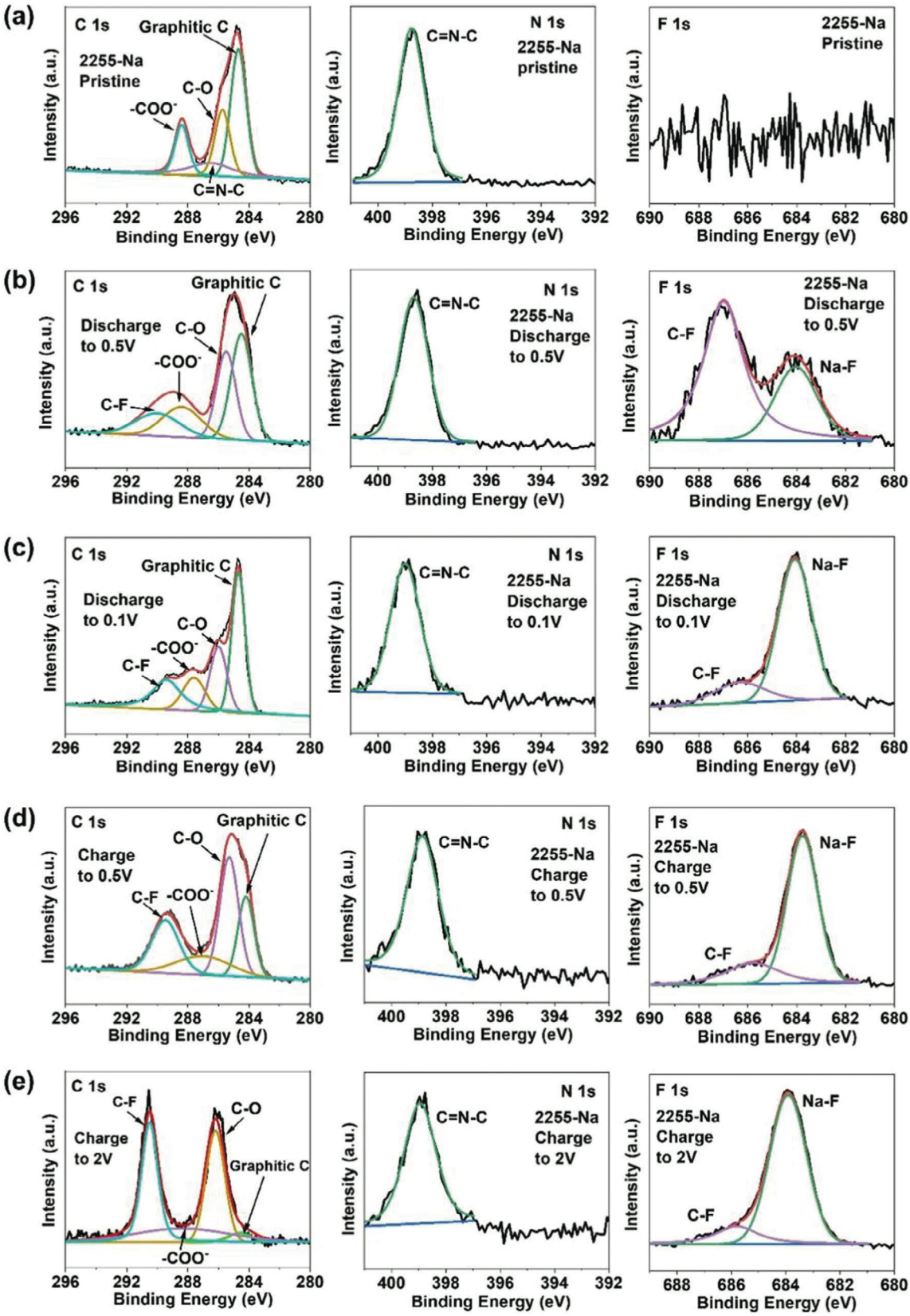

Figure 6. C 1s, N 1s, and F 1s XPS spectra of a) pristine 2255-Na anode, b) 2255-Na anode discharged to 0.5 V, c) 2255-Na anode discharged to 0.1 V, d) 2255-Na anode charged to 0.5 V, e) 2255-Na anode charged to 2 V.

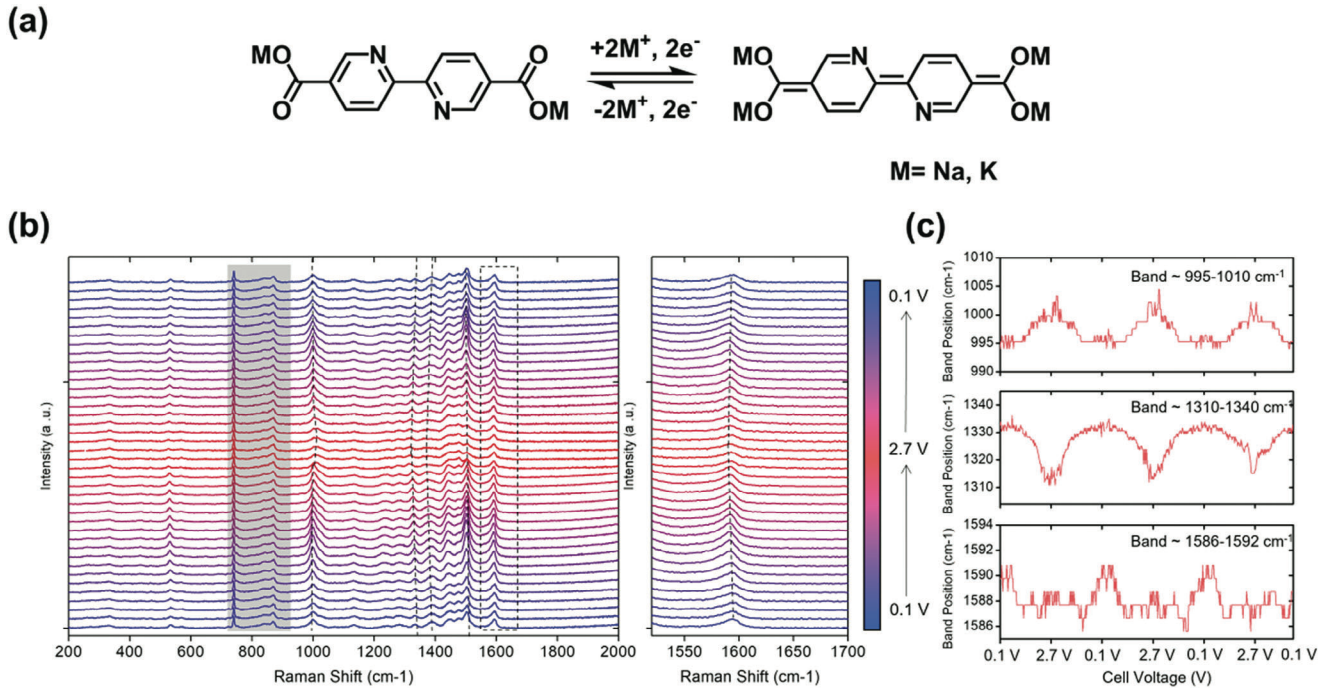

Figure 7. Mechanism study. a) The redox reaction mechanism of 2255-Na/K compounds. b) Operando Raman spectroscopic evolution of the 2255-Na electrode. The shady area indicates Raman bands of electrolytes. Raman bands that demonstrate significant evolution are labeled with dash lines. A zoom-in plot of the band at ≈1586–1592 cm^{-1} included in the dashbox is shown to highlight the subtle band shift. c) Quantified band position shift of three major bands with obvious evolution.

Raman spectroscopic evolution of the 2255-Na electrode within one cycle. The interval of each spectrum corresponds to a voltage interval of 0.13 mV. A few major features are observed in the evolution. First, the high wavenumber band at ≈1590 cm^{-1} demonstrate a moderate red shift upon electrochemical oxidation, as shown in the zoom-in plots of Figure 7b. The shift is mostly likely caused by the conversion from the stretching vibration of C = C terminal double bond (higher wavenumber) to the asymmetric stretching of carboxylate ion (lower wavenumber). In the meantime, the band at ≈1470 cm^{-1} greatly decreases in intensity with elevated voltages. Such a change could be a result of the decrease of C-O- bond at the C = C terminal that converts to carboxylate ions upon removal of electrons. The fingerprint region below 1400 cm^{-1} also demonstrates significant changes. The bands at ≈1320 and ≈1380 cm^{-1} display considerable red shift upon oxidation, which can be a result of the lower C-H bending vibration of fully conjugated pyridine ring than that of N-containing diene. Additionally, a significant band at ≈1000 cm^{-1} exhibits an obvious blue shift upon oxidation. It may correspond to the hardening of the conjugate ring when the N-containing diene is converted to pyridine rings.

Besides the general spectra evolution behavior described above, we extended the analyses to the three consecutive cycles and performed quantified spectroscopic analyses to examine the quantitative correlation. The colormap spectra of the evolution is shown in Figure S16 (Supporting Information), demonstrating highly reversible and coherent band position and intensity changes. The band positions of three key features, including the bands at ≈995–1010, ≈1310–1340, and ≈1586–1592 cm^{-1}, are quantified and summarized in Figure 7c. The "noisy" feature of the band position evolution originates from the automatic band position extraction from 540 spectra. The shifts of different bands as a function of cell voltage are "in-phase", which indicates that these band evolutions are driven by one common mechanism. Moreover, the high periodicity of the evolution also supports the reversibility of the energy storage mechanism.

The *ex situ* XRD (Figure S17, Supporting Information) measurements of 2255-Na at different charge/discharge potential stages were also performed. For XRD tests, the polyimide (PI) tape was used to isolate the electrodes from the air, and the tape has a large broad peak from 10 to 30 degrees (Figure S17, Supporting Information). *Ex situ* XRD was used to monitor the crystalline structure evolution of the first cycle. As shown in Figure S17 (Supporting Information), the 2255-Na anode at 0.1 V shows a large difference from the pristine electrode, indicating crystal structure change after sodiation. Most XRD peaks can be recovered after charging back to 2 V, while the peak at ≈29 degree disappears, due to its intensity decrease and overlap with the strong and broad peak of the PI tape. Therefore, the *in situ* Raman spectroscopy and *ex situ* XRD results confirm the redox reaction between carboxylate groups in 2255-Na and sodium ions/electrons, as well as the high reversibility of the redox reaction.

Due to the superior electrochemical performance of the 2255-Na anode in half cells of NIBs, it was coupled with a p-type polymer cathode, PANI, to explore the full cell performance of all-organic batteries. The PANI cathode undergoes an anion-insertion mechanism in rechargeable batteries, providing a high redox potential above 3 V versus Na/Na^+. To match the capacity with the 2255-Na anode for the full cell measurements, the electrochemical performance of the PANI cathode is investigated.

As shown in Figure S18a (Supporting Information), the PANI cathode exhibits a pair of redox plateaus at ≈3.2 V. Figure S18b (Supporting Information) shows that the initial specific capacity of the PANI cathode is 55.2 mAh g^{-1} at the current density of 50 mA g^{-1}, and it gradually increases to 155.4 mAh g^{-1} after a few cycles and retains at 140.2 mAh g^{-1} after 100 cycles, demonstrating high specific capacity and good cycling stability. The all-organic batteries based on the 2255-Na anode, the PANI cathode, and a 2M $NaPF_6$ in DEGDME electrolyte was tested. **Figure** 8a,b shows the electrochemical performance of the all-organic NIB at room temperature. The current densities and capacity of the full cell are calculated based on the total mass of the 2255-Na anode and the PANI cathode. As shown in Figure 8a,b, the all-organic NIB exhibits superior electrochemical performance at 50 mA g^{-1}, the all-organic NIB delivers an initial reversible capacity of 107.3 mAh g^{-1} and retains at 97.2 mAh g^{-1} after 300 cycles, corresponding to a very slow capacity decay rate of 0.034% per cycle.

Since the all-organic NIB exhibits impressive performance at room temperature, we further investigate the electrochemical performances at high temperatures. To improve the thermal stability of the electrolyte, tetraethylene glycol dimethyl ether (TEGDME) with a high boiling point of 275 °C was applied as a co-solvent in the DEGDME-based electrolyte to increase its boiling point based on Raoult's law. The new electrolyte is 2 M $NaPF_6$ in TEGDME: DEGDME = 1:3 (v/v, which is briefly called TD13). To investigate the thermal stability of the concentrated electrolyte, equivalent amount of TD13, 2M $NaPF_6$ in DEGDME, 1M $NaPF_6$ in dimethoxyethane (DME), and 1M $NaPF_6$ in ethylene carbonate/diethyl carbonate (EC/DEC) electrolytes were heated at 100 °C. As shown in Figure S19a,b (Supporting Information), all the electrolytes are clear solutions without any precipitation before the heat treatment. However, they behaved differently after 24h: TD13 remained clear and the same volume, while 2M $NaPF_6$ in DEGDME had a slight volume decrease, suggesting that part of the solvent was evaporated. In sharp contrast, 1 M $NaPF_6$ in DME and (4) 1 M $NaPF_6$ in EC/DEC electrolytes were dried out. Hence, further characterizations of TD13 such as the electrochemical stability window and ionic conductivity were conducted for the high-temperature battery tests. Figure S20a (Supporting Information) shows the result of the electrochemical stability window test. The cathodic and anodic peaks near 0 V stand for the plating and stripping of Na metal. Since the curve is horizontal from 0.5 to 4 V, it proves that the TD13 electrolyte is stable in the cutoff window from 0–4 V for the all-organic battery test. According to the literature, the equation to calculate ionic conductivity is:

$$\sigma = \frac{L}{R_b A} \tag{1}$$

where L, R_b, and A represent the thickness, the bulk resistance, and the effective area of the separator, respectively. R_b was obtained by EIS under frequencies ranging from 10.0 Hz to 1.0 MHz. From the EIS of the cell (Figure S20b, Supporting Information), the bulk resistance R_b is 8.1 Ω. The effective area (A) of the separator is 0.785 cm^2. The average thickness (L) of the separator is 461.5 µm as measured by SEM in Figure S20c (Supporting Information). Thus, based on the equation and the parameters obtained from the experiments, the ionic conductivity of the TD13 electrolyte is 7.2×10^{-3} S cm^{-1}. Therefore, the TD13 electrolyte has a wide electrochemical stability window and high ionic conductivity for the high-temperature battery tests.

The cyclic stability tests of the all-organic batteries were performed at 60 °C, 80 °C, and 100 °C. As shown in Figure 8c,d, the all-organic batteries delivered a specific capacity of 97.6 mAh g^{-1} at 50 mA g^{-1}, and the capacity was retained at 84.2 mAh g^{-1} after 200 cycles at 60 °C. As shown in Figure 8e, the galvanostatic charge/discharge curves at 50 mA g^{-1} showed a pair of sloping plateaus centered at 2.2 V with an initial capacity of 90.1 mAh g^{-1} at 80 °C. In the long-term cycling test, a reversible capacity of 79.4 mAh g^{-1} was retained after 200 cycles (Figure 8f), demonstrating high durability at 80 °C. Then, the testing temperature was further enhanced to 100 °C. The cell still delivered an initial capacity of 80.4 mAh g^{-1}, and a reversible capacity of 58.3 mAh g^{-1} was retained after 100 cycles. These results prove the outstanding high-temperature performance of the PANI||2255-Na all-organic batteries. Therefore, the 2255-Na anode and TD-13 electrolyte show great promise for the applications in high-temperature batteries.

3. Conclusion

In conclusion, 2255-Na is a promising organic anode material for NIBs due to high stability caused by the aromaticity of the planar extended conjugation structure. Compared with the other twisted compounds (2233-Na and BPDC-Na) and the planar 2266-Na, which suffer from large steric hindrance, non-aromaticity, or high solubility in the electrolyte, 2255-Na provides the highest initial reversible capacity, longest cycle life, and fastest kinetics. The excellent performance of 2255-Na is attributed to the planar spatial structure and proper distance of functional groups. The interfacial chemistry and reaction mechanisms were exploited by XPS and in situ Raman spectroscopy, confirming the formation of a stable NaF-rich SEI layer and the reversible redox reaction between carboxylate groups and Na ions/electrons. More importantly, an all-organic battery based on a 2255-Na anode, a PANI cathode, and an ether-based electrolyte was achieved and exhibited exceptional electrochemical performance at ambient and high temperatures, demonstrating great promise for developing fast-charging and high-temperature batteries. Therefore, this work demonstrates that developing planar organic electrode materials with extended conjugation structures is an effective strategy to achieve affordable, sustainable, and high-performance batteries.

4. Experimental Section

Material Synthesis: 2,2'-bipyridine-5,5'-dicarboxylic acid, 2,2'-bipyridine-3,3'-dicarboxylic acid, and 4,4'-biphenyl dicarboxylic acid were purchased from TCI America, and they were used as received. 2,2'-bipyridine-6,6'-dicarboxylic acid was prepared by the oxidation reaction using 6,6'-bimethyl-2,2'-bipyridine and $KMnO_4$. The synthetic process is as follows: 6,6'-bimethyl-2,2'-bipyridine (0.85 g, 5 mmol) was dissolved in 50 mL distilled water. Potassium permanganate (2.37 g, 15 mmol) was added into the solution, and the resulting mixture was heated at reflux for 12 h. A brown precipitate (MnO_2) was isolated by filtration, and the filtrate was extracted with ether to remove unreacted starting material. The concentrated hydrochloric acid was added into the filtrate to form the precipitate, which was recrystallized using water. 2,2'-bipyridine-6,6'-dicarboxylic acid was collected as a white powder.

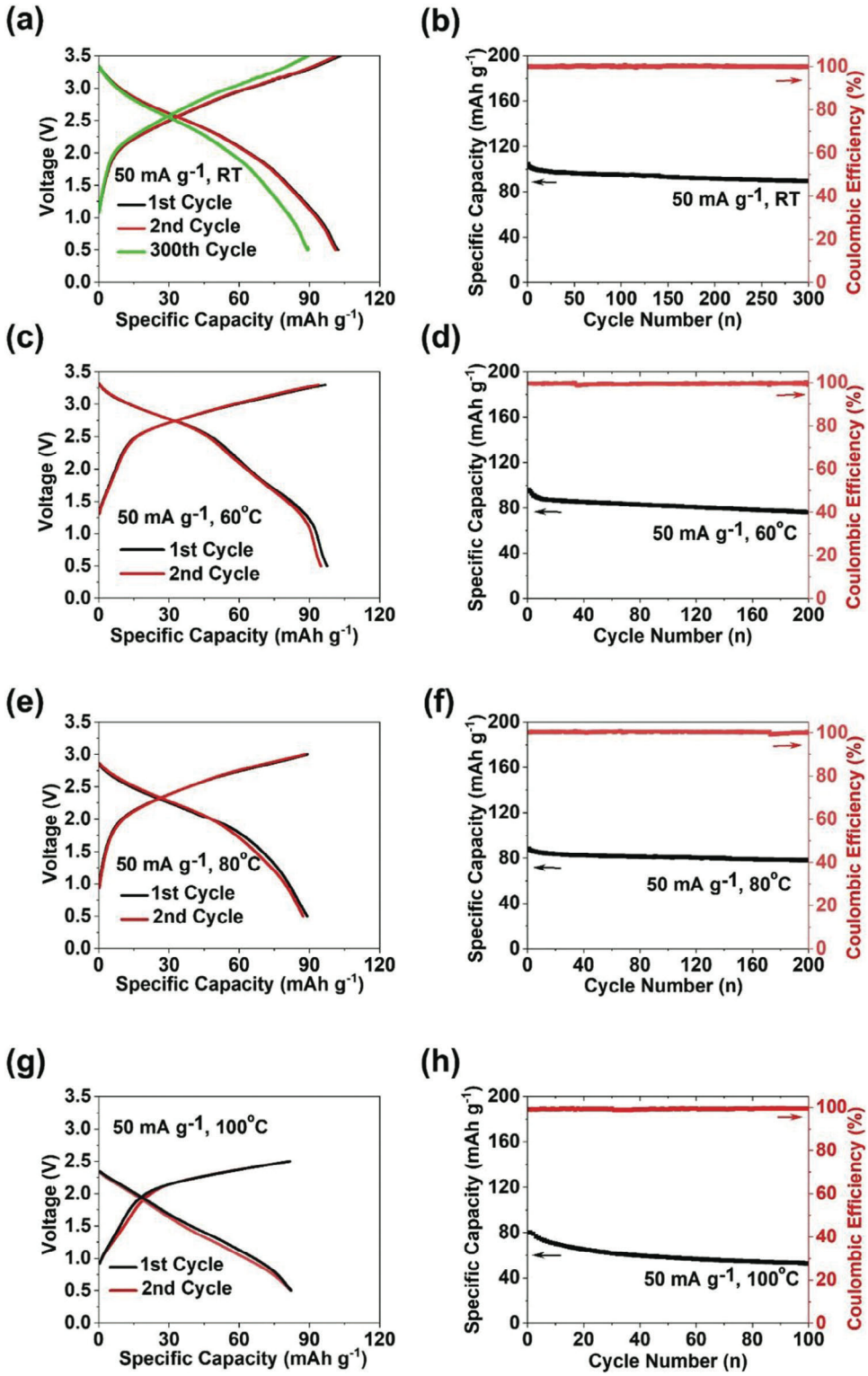

Figure 8. Electrochemical performances of PANI||2255-Na full cells at the current density of 50 mA g^{-1} under different temperatures. a) Galvanostatic charge-discharge curves at room temperature and b) cycle life and Coulombic efficiency at room temperature; c) Galvanostatic charge-discharge curves at 60 °C and d) cycle life and Coulombic efficiency at 60 °C; e) Galvanostatic charge-discharge curves of 80 °C and f) cycle life and Coulombic efficiency at 80 °C; g) Galvanostatic charge-discharge curves at 100 °C and h) cycle life and Coulombic efficiency at 100 °C.

2266-Na, 2255-Na, 2233-Na, and BPDC-Na were synthesized as follows:[31,33] The corresponding acids were dissolved in the absolute ethanol with sodium hydroxide in two equivalents. The solutions were stirred for 24 h under ambient environment, then the precipitates were collected by vacuum filtration. The precipitates were washed with absolute ethanol and dried in the vacuum oven at 100 °C overnight. All the products were white powders.

Material Characterizations: X-ray diffraction (XRD) pattern was recorded by Rigaku MiniFlex 600 using CuKα radiation; Raman measurements were performed on a Horiba Jobin Yvon Labram Aramis using a 532 nm diode-pumped solid-state laser, attenuated to give ≈900 µW power at the sample surface; Fourier transform infrared spectroscopy (FTIR) was recorded by Agilent Cary 630 FTIR Instrument; Scanning Electron Microscope (SEM) images were taken by JEOL JSM-IT500HR InTouchScope SEM instrument (Japan); Nuclear magnetic resonance spectroscopy (NMR) tests were performed with Bruker Ascend 400 NMR spectrometer. Mass spectroscopy (MS) tests were done with Sciex QTRAP 4500. Samples were prepared at a concentration of 1 microgram mL^{-1} in water and directly infused into the mass spectrometer. TEM images were taken by JEOL JEM-1400F; XPS measurements were carried out at a PHI 5000 VersaProbe II system (Physical Electronics) spectrometer, which is equipped with a hemispherical analyzer. The spectrometer is attached to the Ar glovebox and sample transfer was directly through it to avoid any contact of the samples with air and moisture. Monochromatic Al-Kα excitation ($h\nu$ = 1486.6 eV) was used at power of 25 W, additionally applying a low-energy electron charge neutralizer. The high-resolution spectrum of each element was collected with a pass energy of 23.25 eV in an analysis area of 100*100 µm.

Electrochemical Measurements: The product compounds were blended with carbon black (CB) and sodium alginate (SA) binder to form a slurry with the weight ratio of 6:3:1. The electrodes were prepared by casting the slurry onto copper or aluminum foil using a doctor blade and dried in a vacuum oven at 100 °C overnight. The copper foil coated with slurry was punched into rounded electrodes with an area mass loading of ≈1.5 mg cm^{-2}. The sodium batteries used for electrochemical tests were coin cells and assembled with sodium metal as the counter electrode, 2 M $NaPF_6$ in DEGDME electrolyte, and glass-fibre as the separator. The electrochemical performance of the cells was tested by Arbin battery test station (LBT20084, Arbin Instruments, USA). Cyclic voltammograms were examined with Gamry Interface 1010 E Potentiostat/ Galvanostat/ ZRA with scan rates from 0.1 to 2 mV s^{-1}. Impedance analysis was performed by the same Gamry instrument. In GITT test, the battery was discharged to 0.1 V, and then charged back to 2 V at the current density of 50 mA g^{-1}. During the cycling process, the battery was discharged or charged for 30 min, and then rest for 3 h to reach the equilibrium potentials. The high mass loading electrodes were applied for XRD tests in order to enhance the strength of the signal of XRD, which were fabricated by using polytetrafluoroethylene (PTFE) as the binder, and the ratio of 2255-Na, CB and PTFE was still 6:3:1. The ratio of electrodes in ex-situ XRD tests are changed to 8:1:1 to decrease the effect of CB in the tests.

Operando Raman spectroscopy was performed using a Renishaw In-Via microspectrometer. A 633 nm He-Ne Laser (8 mW) was used as excitation source. The configuration of operando Raman cell was described elsewhere.[56] The operando Raman measurement was driven by a cyclic voltammetry test with a scan rate of 0.2 V S^{-1}.

The theoretical capacity values of 2255-Na, 2233-Na, and 2266-Na were calculated based on the equation:

$$C_{th} = \frac{n \times F}{M} \quad (2)$$

where n is the number of electrons transferred, F is Faraday constant, M is the molar mass of the molecule. Based on the reaction mechanism, all the three halogenated sodium carboxylates undergo a two-electrons reaction, thus n is 2. For 2255-Na, 2233-Na, and 2266-Na, their molar masses are all 288.2 g mol^{-1}, thus their theoretical capacities are 186.1 mAh g^{-1}. Similarly, the theoretical capacity of BPDC-Na is 188.7mAh g^{-1}, respectively.

The cell used for steady potential test was coin cell assembled with sodium metal as the counter electrode, to avoid the influence from active material, stainless steel mesh was applied as the working electrode, 2 M $NaPF_6$ in TD13 was the electrolyte, glass-fiber was the separator. The cell was performed a CV test with the voltage window of −0.5 to 4 V. The same cell combination was also used in the EIS test of the new electrolyte.

Computational Methods: Density functional theory calculations were carried out using the Amsterdam Density Functional (ADF) 2020 package at the B3LYP/TZ2P level of theory. Density functional theory (DFT) calculations were performed using Gaussian 16 to determine the potential energy surface (PES) and optimized structures of the four monomers. The ωB97X-D /6-311++G(d,p) level of theory was used for these calculations and the Na^+ ions were replaced by hydrogen in the PES calculations to reduce the computational cost. The C-C' torsion angle was scanned from 0° to 180° in 10° intervals, with all other bond lengths and angles optimized at each step.

Supporting Information

Supporting Information is available from the Wiley Online Library or from the author.

Acknowledgements

This work was supported by the US National Science Foundation Award No. 2154145. The authors also acknowledge the support from the Quantum Science & Engineering Center and College of Science at George Mason University. The authors thank for the technical support of mass spectroscopy from Dr. Michael Girgis and Dr. Mikell Paige from Department of Bioengineering at George Mason University. The authors gratefully acknowledge support from the Post Test Facility at Argonne National Laboratory, which is operated for DOE Vehicle Technologies Office (VTO) by UChicago Argonne, LLC, under contract number DE-AC02-06CH11357.

Conflict of Interest

The authors declare no conflict of interest.

Data Availability Statement

The data that support the findings of this study are available from the corresponding author upon reasonable request.

Keywords

anodes, carboxylate, high-temperature batteries, Na-ion batteries, planar structures, spatial effect

Received: September 15, 2023
Revised: October 27, 2023
Published online: November 16, 2023

[1] J. Huang, S. Li, E. Y. Kim, L. Cheng, G.-L. Xu, K. Amine, C. Wang, C. Luo, *Small Struct* **2023**, 2300211.
[2] M. Mohammadiroudbari, J. Huang, E. Y. Kim, Z. Yang, F.u Chen, C. Luo, *J. Mater. Chem. A* **2023**, *11*, 16636.
[3] L. Liang, X. Chen, W. Yuan, H. Chen, H. Liao, Y. Zhang, *ACS Appl. Mater. Interfaces* **2021**, *13*, 25410.

[4] P. K. Nayak, L. Yang, W. Brehm, P. Adelhelm, *Angew. Chemie – Int. Ed.* **2018**, *57*, 102.
[5] C. Delmas, *Adv. Energy Mater.* **2018**, *8*, 1703137.
[6] J. Deng, W.-B. Luo, S.-L. Chou, H.-K. Liu, S.-X. Dou, *Adv. Energy Mater.* **2018**, *8*, 1701428.
[7] Y. Liu, Y. Xu, Y. Zhu, J. N. Culver, C. A. Lundgren, K. Xu, C. Wang, *ACS Nano* **2013**, *7*, 3627.
[8] J. Wang, C. Luo, T. Gao, A. Langrock, A. C. Mignerey, C. Wang, *Small* **2015**, *11*, 473.
[9] S. Baddi, U. Ghani, J. Huang, Q. Liu, C.-L. Feng, *Energy Storage Mater.* **2023**, *59*, 102786.
[10] C. Luo, J. Wang, X. Fan, Y. Zhu, F. Han, L. Suo, C. Wang, *Nano Energy* **2015**, *13*, 537.
[11] C. Wang, Y. Xu, Y. Fang, M. Zhou, L. Liang, S. Singh, H. Zhao, A. Schober, Y. Lei, *J. Am. Chem. Soc.* **2015**, *137*, 3124.
[12] C. Ma, X. Zhao, L. Kang, K.-X. Wang, J.-S. Chen, W. Zhang, J. Liu, *Angew. Chemie* **2018**, *130*, 9003.
[13] T. B. Schon, B. T. Mcallister, P.-F. Li, D. S. Seferos, *Chem. Soc. Rev.* **2016**, *45*, 6345.
[14] K. Jia, L. Zhu, F. Wu, *ChemSusChem* **2021**, *14*, 3124.
[15] Q. Zhao, Y. Lu, J. Chen, *Adv. Energy Mater.* **2017**, *7*, 1601792.
[16] B. Häupler, A. Wild, U. S. Schubert, *Adv. Energy Mater.* **2015**, *5*, 1402034.
[17] K. Jia, J. Zhang, P. Hu, L. Zhu, X. Li, X. Liu, R. He, F. Wu, *J. Colloid Interface Sci.* **2022**, *623*, 637.
[18] S. Muench, A. Wild, C. Friebe, B. Häupler, T. Janoschka, U. S. Schubert, *Chem. Rev.* **2016**, *116*, 9438.
[19] T. B. Schon, A. J. Tilley, C. R. Bridges, M. B. Miltenburg, D. S. Seferos, *Adv. Funct. Mater.* **2016**, *26*, 6896.
[20] Z. Luo, L. Liu, J. Ning, K. Lei, Y. Lu, F. Li, J. Chen, *Angew. Chemie – Int. Ed.* **2018**, *57*, 9443.
[21] J. Xie, W. Chen, G. Long, W. Gao, Z. J. Xu, M. Liu, Q. Zhang, *J. Mater. Chem. A* **2018**, *6*, 12985.
[22] D. Chen, A.-J. Avestro, Z. Chen, J. Sun, S. Wang, M. Xiao, Z. Erno, M. M. Algaradah, M. S. Nassar, K. Amine, Y. Meng, J. F. Stoddart, *Adv. Mater.* **2015**, *27*, 2907.
[23] K. Holguin, M. Mohammadiroudbari, K. Qin, C. Luo, *J. Mater. Chem. A* **2021**, *9*, 19083.
[24] Q. Zhao, J. Wang, Y. Lu, Y. Li, G. Liang, J. Chen, *Angew. Chemie – Int. Ed.* **2016**, *55*, 12528.
[25] C. Luo, O. Borodin, X. Ji, S. Hou, K. J. Gaskell, X. Fan, J. Chen, T. Deng, R. Wang, J. Jiang, C. Wang, *Proc. Natl. Acad. Sci. USA* **2018**, *115*, 2004.
[26] H. Zhao, J. Wang, Y. Zheng, J.u Li, X. Han, G. He, Y. Du, *Angew. Chemie – Int. Ed.* **2017**, *56*, 15334.
[27] K. Sakaushi, E. Hosono, G. Nickerl, T. Gemming, H. Zhou, S. Kaskel, J. Eckert, *Nat. Commun.* **2013**, *4*, 1485.
[28] C. Luo, G.-L. Xu, X. Ji, S. Hou, L. Chen, F. Wang, J. Jiang, Z. Chen, Y. Ren, K. Amine, C. Wang, *Angew. Chemie* **2018**, *130*, 2929.
[29] E. Castillo-Martínez, J. Carretero-González, M. Armand, *Angew. Chemie – Int. Ed.* **2014**, *53*, 5341.
[30] M. López-Herraiz, E. Castillo-Martínez, J. Carretero-González, J. Carrasco, T. Rojo, M. Armand, *Energy Environ. Sci.* **2015**, *8*, 3233.
[31] K. Qin, K. Holguin, M. Mohammadiroudbari, C. Luo, *Chem. Commun.* **2021**, *57*, 2360.
[32] C. Luo, X. Fan, Z. Ma, T. Gao, C. Wang, *Chem* **2017**, *3*, 1050.
[33] C. Luo, J. J. Shea, J. Huang, *J. Power Sources* **2020**, *453*, 227904.
[34] G. Zhao, Y. Zhang, Z. Gao, H. Li, S. Liu, S. Cai, X. Yang, H. Guo, X. Sun, *ACS Energy Lett.* **2020**, *5*, 1022.
[35] S. Gu, S. Wu, L. Cao, M. Li, N. Qin, J. Zhu, Z. Wang, Y. Li, Z. Li, J. Chen, Z. Lu, *J. Am. Chem. Soc.* **2019**, *141*, 9623.
[36] J. J. Shea, C. Luo, *ACS Appl. Mater. Interfaces* **2020**, *12*, 5361.
[37] Y. Wu, Y. Chen, M. Tang, S. Zhu, C. Jiang, S. Zhuo, C. Wang, *Chem. Commun.* **2019**, *55*, 10856.
[38] K. Qin, J. Huang, K. Holguin, C. Luo, *Energy Environ. Sci.* **2020**, *13*, 3950.
[39] W. Luo, M. Allen, V. Raju, X. Ji, *Adv. Energy Mater.* **2014**, *4*, 1400554.
[40] X. Han, G. Qing, J. Sun, T. Sun, *Angew. Chemie – Int. Ed.* **2012**, *51*, 5147.
[41] Y. Shan, Y. He, N. Yang, X. Zhu, H. Liu, H. Jiang, C. Li, *Small* **2022**, *18*, 2270004.
[42] Y. Shan, Y. He, Y. Gu, Y. Sun, N. Yang, H. Jiang, F. Wang, C. Li, D.-E. Jiang, H. Liu, X. Zhu, S. Dai, *Chem. Eng. J.* **2022**, *430*, 133055.
[43] N.a Yang, Y. Gu, Y. Shan, C. Tian, L. Yang, H. Jiang, H. Liu, X. Zhu, S. Dai, *ACS Macro Lett.* **2022**, *11*, 60.
[44] J. Huang, K. I. E. Callender, K. Qin, M. Girgis, M. Paige, Z. Yang, A. Z. Clayborne, C. Luo, *ACS Appl. Mater. Interfaces* **2022**, *14*, 40784.
[45] Y. Bo, W. Wu, R. Guo, M. Cao, Y. Liang, M.i Wang, W. Yu, L. Zhang, J. Zhang, *Electrochim. Acta* **2022**, *405*, 139628.
[46] V.-V. V. Hugo, H.-S. M. Alejandro, V.-S. A. María, R.-H. María, L.-R. M. Antonio, P.-O. M. Guadalupe, M.-G. M. Antonio, A.-H. Fernando, A. Víctor, C.-A. Diego, Á. Enrique, *Comput. Chem.* **2019**, *7*, 1.
[47] F. Ge´Nin, F. Quilès, A. Burneau, *Phys. Chem. Chem. Phys.* **2001**, *3*, 932.
[48] H. Gao, L. Xue, S. Xin, J. B. Goodenough, *Angew. Chemie* **2018**, *130*, 5547.
[49] J. Huang, J. Lu, Y. Zhang, S. Xie, G. Lin, W. Lin, P. Zhuang, Z. Zhu, S. Guo, S. Zhang, Q. Ge, X. Zhang, W. Cai, *J. Phys. Chem. C* **2021**, *125*, 14891.
[50] C. Luo, X. Ji, S. Hou, N. Eidson, X. Fan, Y. Liang, T. Deng, J. Jiang, C. Wang, *Adv. Mater.* **2018**, *30*, 1706498.
[51] C. Wang, Y. Xu, Y. Fang, M. Zhou, L. Liang, S. Singh, H. Zhao, A. Schober, Y. Lei, *J. Am. Chem. Soc.* **2015**, *137*, 3124.
[52] K. Qin, K. Holguin, J. Huang, M. Mohammadiroudbari, F.u Chen, Z. Yang, G.-L. Xu, C. Luo, *Adv. Sci.* **2022**, *9*, 2106116.
[53] Y. Liang, C. Luo, F. Wang, S. Hou, S.z-C. Liou, T. Qing, Q. Li, J. Zheng, C. Cui, C. Wang, *Adv. Energy Mater.* **2019**, *9*, 1802986.
[54] V. Augustyn, J. Come, M. A. Lowe, J. W. Kim, P.-L. Taberna, S. H. Tolbert, H. D. Abruña, P. Simon, B. Dunn, *Nat. Mater.* **2013**, *12*, 518.
[55] D. Lin-Vien, N. B. Colthup, W. G. Fateley, J. G. Grasselli, *The handbook of infrared and Raman characteristic frequencies of organic molecules*, Elsevier, New York **1991**.
[56] D. Chen, J.-H. Wang, T.-F. Chou, B. Zhao, M. A. El-Sayed, M. Liu, *J. Am. Chem. Soc.* **2017**, *139*, 7071.